

# Time-series Paschen- $\beta$ spectroscopy of SU Aurigae

Ryuichi Kurosawa\*, Tim J. Harries and Neil H. Symington

*School of Physics, University of Exeter, Stocker Road, Exeter EX4 4QL*

Dates to be inserted

## ABSTRACT

We present time-series echelle spectra of the Pa $\beta$  line of the T Tauri star SU Aur, observed over three consecutive nights. The line shows strong variability ( $\sim 10$  per cent) over the velocity range ( $100 \text{ km s}^{-1}$ ,  $420 \text{ km s}^{-1}$ ) in the red broad absorption component, and weaker variability ( $\sim 2$  per cent) over the velocity range ( $-200 \text{ km s}^{-1}$ ,  $0 \text{ km s}^{-1}$ ) in the blue wing. The variability in the velocity range ( $-200 \text{ km s}^{-1}$ ,  $0 \text{ km s}^{-1}$ ) is correlated with that in ( $200 \text{ km s}^{-1}$ ,  $400 \text{ km s}^{-1}$ ), and the variability in these velocity ranges anti-correlates with that in ( $0 \text{ km s}^{-1}$ ,  $100 \text{ km s}^{-1}$ ). The mean spectrum from the second night shows a suggestion of a blue-shifted absorption component at about  $-150 \text{ km s}^{-1}$ , similar to that found in the H $\alpha$  and H $\beta$  lines. We find the position of the subpeak in the red absorption component changes steadily with time, and its motion modulates on half the rotational period. We also find that the modulation of the line equivalent width is associated with a half and a third of the rotational period, which is consistent with the surface Doppler images of SU Aur. Radiative transfer models of a rotationally modulated Pa $\beta$  line, produced in the shock-heated magnetospheric accretion flow, are also presented. Models with a magnetic dipole offset reproduce the overall characteristics of the observed line variability, including the line equivalent width and the motion of the subpeak in the red absorption trough.

**Key words:** stars:formation – stars: individual: SU Aur – circumstellar matter – stars: pre-main-sequence

## 1 INTRODUCTION

T Tauri stars (TTS) are young ( $< \sim 3 \times 10^6$  yrs, Appenzeller & Mundt 1989) low-mass stars, and are thought to be the progenitors of solar-type stars. Classical T Tauri stars (CTTS) exhibit strong H $\alpha$  emission, and typically have spectral types of F–K. Some of the most active CTTS show emission in higher order Balmer lines and metal lines (e.g. Ca II, H and K). They also exhibit an excess amount of continuum flux in the ultraviolet (UV) and infrared (IR).

Line profile studies of CTTS show evidence for both outflows and inflows, as seen in the blue-shifted absorption features in H $\alpha$  profiles (e.g. Herbig 1962) and the inverse P Cygni (IPC) profiles (e.g. Kenyon et al. 1994; Edwards et al. 1994) respectively. Typical mass-loss rates of CTTS are about  $10^{-9} \text{ M}_{\odot} \text{ yr}^{-1}$  to  $10^{-7} \text{ M}_{\odot} \text{ yr}^{-1}$  (e.g. Kuhl 1964; Edwards et al. 1987; Hartigan et al. 1995), and mass-accretion rates range from  $10^{-9} \text{ M}_{\odot} \text{ yr}^{-1}$  to  $10^{-7} \text{ M}_{\odot} \text{ yr}^{-1}$  (e.g. Kenyon & Hartmann 1987; Bertout, Basri, & Bouvier 1988; Gullbring et al. 1998).

In the currently favoured model of accretion on to CTTS, the accretion discs are disrupted by the stellar magnetosphere which channel the gas from the disc on to the stellar surface (e.g. Uchida & Shibata 1985; Koenigl 1991;

Collier Cameron & Campbell 1993; Shu et al. 1994a). This picture of the accretion flows is supported by the observation that CTTS have relatively strong ( $\sim 10^3 \text{ G}$ ) magnetic fields (e.g. Johns-Krull, Valenti, Hatzes, & Kanaan 1999; Guenther & Emerson 1996; Symington et al. 2004b) and by radiative transfer models which reproduce the gross characteristics of the observed profiles for some TTS (e.g. Muzerolle, Calvet, & Hartmann 2001).

SU Aurigae is a bright ( $J \sim 7$ , Chakraborty & Ge 2004) young star with a G2 spectral type (Herbig 1960), and has been classified either as a CTTS (e.g. Giampapa et al. 1993; Bouvier et al. 1993) or early-type TTS (e.g. Herbst et al. 1994). It is also the prototype ‘SU Aur type’ (Herbig & Bell 1988). Based on modelling of the spectral energy distribution (SED), SU Aur is known to have an accretion disc ( $\sim 400 \text{ au}$ ) along with an outer envelope (e.g. Akeson et al. 2002). Near-infrared coronagraphic observations of Nakajima & Golimowski (1995) and Grady et al. (2001) have shown that the object is associated with a reflection nebula and outflows. Most recently, Chakraborty & Ge (2004) have presented high resolution (0.3 arcsec)  $J$ -,  $H$ - and  $K$ -band adaptive optics images displaying nebulosity with a disc-like structure around SU Aur.

SU Aur has been a subject of a number of variability studies, mainly in the optical, e.g. Giampapa et al. (1993), Johns & Basri (1995), Petrov et al. (1996), Oliveira et al. (2000) and most recently

\* E-mail: rk@astro.ex.ac.uk

Unruh et al. (2004). The  $H\alpha$  line, which is most commonly used for variability studies of TTS, is produced over a large circumstellar volume, and shows evidence of outflow (winds) as well as magnetospheric inflow. Johns & Basri (1995) studied the variability of  $H\alpha$  and  $H\beta$  profiles of SU Aur, and found that the modulation of the wind and the accretion components in the profiles are approximately  $180^\circ$  out of phase. This led them to suggest that the magnetic field axis is slightly tilted with respect to the rotation axis of the star.

The topology of the magnetic field is still in dispute. Despite of the overall success of the dipole field geometry used in explaining many observed features of CTTS, Johns-Krull & Gafford (2002) re-examined the validity of this assumption. They found that observations did not support the relationships between mass, radius, and rotation period that magnetospheric accretion theory predicts under the assumption of a dipolar field, but found better agreement when a non-dipole field topology was used. In addition, for SU Aur, Unruh et al. (2004) found a lack of the circular polarisation across some strong photospheric lines; once again in conflict with the expectations for a large-scale dipole. Further, Oliveira et al. (2000) found the time-lagged behaviour in the variability of some optical lines, and proposed that this can be caused by the presence of an azimuthal component in the magnetosphere.

Near-IR profiles, such as  $\text{Pa}\beta$  and  $\text{Br}\gamma$  are likely to become important probes of accretion in CTTS and their lower-mass counterparts, since they appear to suffer from less contamination by outflows than  $H\alpha$  (e.g. Folha 1998; Folha & Emerson 2001, although see Whelan et al. 2004) and are less affected by dust obscuration, enabling the study of accretion in highly embedded objects. Here we present time-series  $\text{Pa}\beta$  spectra of SU Aur, which we use to probe the accretion geometry. In Section 2 we give details on the observations and the data reduction. The results and analysis are presented in Section 3. Radiative transfer models are computed in an attempt to explain the overall observed variability feature in Section 4. The conclusions are given in Section 5.

## 2 OBSERVATIONS

A total of 503  $\text{Pa}\beta$  ( $\lambda = 1.28181 \mu\text{m}$ ) spectra with a signal-to-noise ratio (S/N) of  $\sim 90$  per pixel (in the continuum) were obtained over 3 nights (2002 December 1–3) at the United Kingdom Infrared Telescope (UKIRT) on Mauna Kea, Hawaii. The approximate temporal sampling rate was one spectrum every 3 minutes.

The Cooled Grating Spectrometer No. 4 (CGS4), a 1–5  $\mu\text{m}$  multi-purpose 2-D grating spectrometer with a  $256 \times 256$  InSb array, with the echelle grating and long camera (300 mm), was used. This provides a velocity resolution (at  $1.28181 \mu\text{m}$ ) of  $\sim 16 \text{ km s}^{-1}$  using  $\sim 1$  pix slit width without the Nyquist stepping. The wavelength range of the echelle spectra is about  $3600 \text{ km s}^{-1}$  providing enough continuum on either side of the line for accurate rectification. Unfortunately there are insufficient photospheric features to perform a veiling correction (but see Section 4.2). Telluric standard stars were observed throughout each night (every 2–3 hours) to correct for instrument response and atmospheric transmission.

The data obtained with CGS4 were reduced using a standard procedure (c.f. Puxley et al. 1992): 1. bias subtraction, 2. flat-field, and 3. optimal extraction (Horne 1986). All spectra were reduced in the same manner, using the ORAC-DR pipeline program. Intrinsic absorption components in the standard stars, used in step 3 to correct for the telluric lines, were subtracted from the original spec-

tra by using the least square fit of the spectra with a combination of two Gaussian functions and a third order polynomial. After the preliminary reduction by the pipeline was finished, a wavelength calibration was performed using a combination of OH sky emission lines and comparison arc lines. Finally we applied heliocentric velocity corrections and shifted the spectra into the rest-frame of SU Aur, adopting the radial velocity measurement ( $+16 \text{ km s}^{-1}$ ) of Herbig & Bell (1988).

## 3 RESULTS

A general overview of the dataset is presented in Fig. 1. The mean spectrum shows a classic inverse P Cygni (IPC) profile, with the blue-wing of the emission component extending to  $-200 \text{ km s}^{-1}$  and the absorption component with maximum depth at  $+100 \text{ km s}^{-1}$  and extending out to  $+200 \text{ km s}^{-1}$ . The peak intensity of the line, relative to the continuum, is about 1.25. Although comparable in strength, the  $\text{Pa}\beta$  profiles of SU Aur presented by Folha & Emerson (2001) show significant emission redwards of the absorption dip, and also have maximum absorption occurring at  $0 \text{ km s}^{-1}$  i.e. they appear to be shifted by  $\sim 90 \text{ km s}^{-1}$  blueward compared to our dataset.

The mean spectra from each night are shown in Fig. 2. It is immediately apparent that the blue side of the profile is more stable than the red, with variability of less than 10 per cent (in continuum units) at the line peak and blueward. There is a suggestion of blue-shifted absorption at about  $-150 \text{ km s}^{-1}$  on the second night. Interestingly, the blue-shifted absorption feature at  $-150 \text{ km s}^{-1}$  is also seen in  $H\alpha$  (Giampapa et al. 1993) and  $H\beta$  (Johns & Basri 1995) profiles, and the modulation period of the absorption feature is identified as the rotational period of SU Aur ( $\sim 3 \text{ d}$ ). The red side of the mean profiles shows strong variability, extending redward to over  $+400 \text{ km s}^{-1}$ . On the final night there is emission on the red side of the absorption trough, and the profile more closely resembles that presented by Folha & Emerson (2001).

The greyscale dynamic spectra (Fig. 1) reveal the gradual changes that occur over a timescale of hours. On the first night there is a feature that accelerates monotonically redward across the absorption trough. On the second night both the red and blue sides of the profile are lower than the mean. Finally, on the third night we see the growth of an emission feature in the absorption dip. The characteristic level of this red-wing variability is about 10 per cent.

### 3.1 Temporal variance spectra

In order to quantify the level and significance of the variability seen in the  $\text{Pa}\beta$  profiles, the temporal variance spectrum (TVS) analysis method proposed by Fullerton, Gies, & Bolton (1996) was applied to the time series spectra from each night separately, and also to all three nights combined. This method statistically compares the deviations in line features with those of the adjacent continuum. In other words, the level of deviation at a given wavelength is computed with a weight function which is inversely proportional to the signal-to-noise (S/N) level of the continuum. By using the definition of Fullerton et al. (1996), the  $j$ -th velocity bin of the TVS, in the limit of high photon-count, can be written as:

$$(\text{TVS})_j = \frac{1}{N-1} \sum_{i=1}^N (S_{ij} - \bar{S}_j)^2 \frac{w_i}{S_{ij}} \quad (1)$$

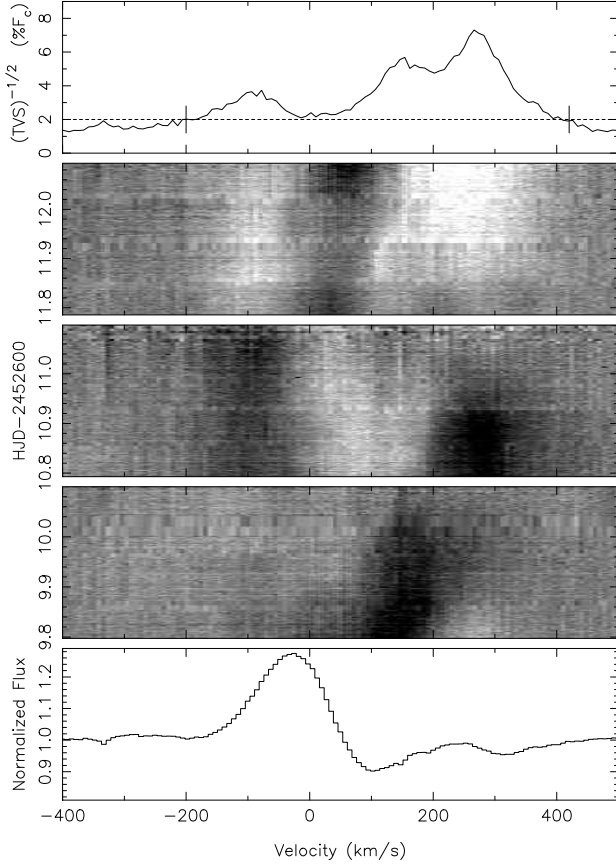


**Figure 1.** The time-series spectra of Pa $\beta$ . The mean spectrum (normalised) of the 503 spectra obtained during the three night (2002 December 1–3) is shown at the bottom. In the middle panels, the quotient spectra (divided by the mean spectrum) as a function of time (HJD – 2452600) are plotted as greyscale images with the colour scaled from 1.1 (white) to 0.9 (black). The temporal deviation spectrum (TVS)<sup>1/2</sup> from the 503 spectra is shown on the top panel (c.f. Section 3.1). In all plots, the horizontal axes are in velocity space in the stellar rest frame. The greyscale images clearly show variability on both red and blue sides of the spectra, but little variability is seen near the line centre. The dashed line in the top panel shows the statistical significance at the 1 per cent level, and it indicates that the velocity range (–200 km s<sup>–1</sup>, 420 km s<sup>–1</sup>) has significant variability.

where  $S_{ij}$  is the signal of the  $j$ -th velocity bin belonging to the  $i$ -th spectrum of a time-series, and  $N$  is the number of observed spectra.  $\bar{S}_j$  is the weighted mean spectrum defined as

$$\bar{S}_j = \frac{1}{N} \sum_{i=1}^N w_i S_{ij} . \quad (2)$$

The weighting factor  $w_i$  for the  $i$ -th spectrum is defined as

$$w_i = \frac{(1/\sigma_{ic}^2)}{\frac{1}{N} \sum_{k=1}^N (1/\sigma_{kc}^2)} \quad (3)$$

where  $\sigma_{ic}$  and  $\sigma_{kc}$  are the noise in the continuum for the  $i$ -th and  $k$ -th spectra.

As mentioned by Fullerton et al. (1996), a more convenient quantity to be plotted is the square root of TVS (temporal deviation spectrum) because (TVS)<sup>1/2</sup> scales linearly with the spectral

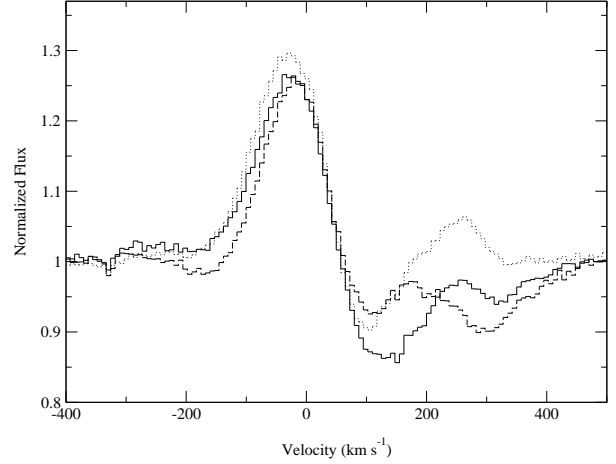


**Figure 2.** Mean spectra from each night: The first night (solid), the second night (dashed), and the third night (dotted). While most of the variability occurs in the red side (50 km s<sup>–1</sup>, 500 km s<sup>–1</sup>) of the line, small yet noticeable changes in flux level can be seen in (–200 km s<sup>–1</sup>, 0 km s<sup>–1</sup>). The flux level at ~250 km s<sup>–1</sup> is below the continuum on the first and the second night, but it is in emission (above the continuum) on the third night. A hint of a blue-shifted absorption component at ~150 km s<sup>–1</sup> is seen on the second night.

deviations; hence, it provides a more accurate impression of the deviation from the variability with respect to the continuum.

Using equation 1, the temporal deviation spectrum of the times-series spectra from each night was computed, and the results were placed in the top panels of Fig. 3. In the same figure, the spectra divided by the mean spectrum of each night (the quotient spectra) and the mean spectrum are shown as a function of time. Similarly, (TVS)<sup>1/2</sup> computed from all three nights is placed in the top of Fig. 1.

The (TVS)<sup>1/2</sup> value which corresponds to one per cent statistical significance (the  $\chi^2$ -probability) is also shown in the same figure as a reference point. In the absence of real variability, the observed (TVS)<sup>1/2</sup> values should be below this level for 99 per cent of time. From the (TVS)<sup>1/2</sup> plot in Fig. 1, we confirm that the line displays strong variability within the velocity range (100 km s<sup>–1</sup>, 420 km s<sup>–1</sup>) in the red wing, and weaker variability within the velocity range (–200 km s<sup>–1</sup>, 0 km s<sup>–1</sup>) in the blue wing. The (TVS)<sup>1/2</sup> plots in Fig. 3 show that the velocity ranges in which the variability is most active change from night to night.

Using the mass ( $M_* = 2.25 M_\odot$ ) and the radius ( $R_* = 3.6 R_\odot$ ) of SU Aur from Cohen & Kuhi (1979), we find its escape velocity to be  $V_{\text{esc}} = (2GM_*/R_*)^{1/2} = 490 \text{ km s}^{-1}$ . This value is an upper-limit for the velocity of the material as it impacts on the stellar surface, and indeed we see that the extent of the red absorption in the line profile is ~420 km s<sup>–1</sup>, and that the maximum velocity of significant variability is ~420 km s<sup>–1</sup>.

### 3.2 Motion of a subpeak in the absorption trough

In the red absorption trough of the mean spectra (see the bottom panels of Fig. 3), we find the presence of a subpeak at  $V \sim 250$ , ~180 and ~260 km s<sup>–1</sup> for the first, second and third nights. We also find the position of the subpeak (indicated by arrows in the same figure) changes during one night. It appears that a main cause of the variability seen in the red-wing (as seen in the greyscale images in the same figures) is due to the motion of this subpeak,

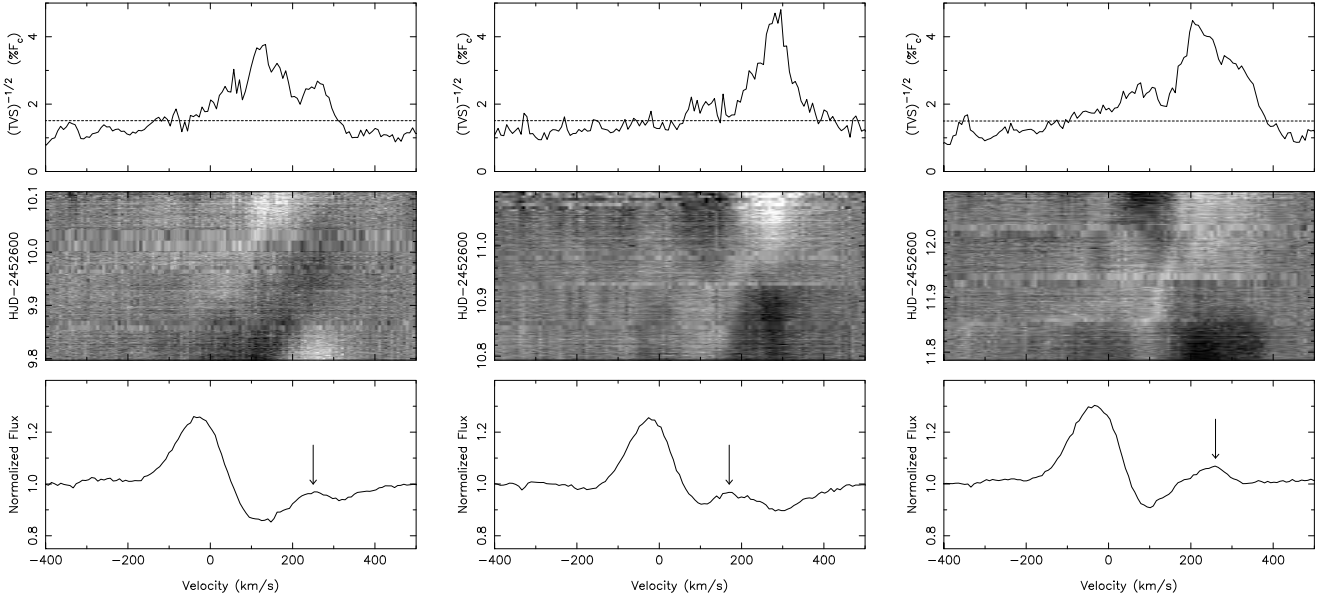


**Figure 3.** The summary of observations from each night (the first night to the third night from left to right respectively). For each night, the normalised mean spectrum (bottom), the quotient spectra (divided by the mean spectrum) (middle) with colour scaled from 1.08 (white) to 0.92 (black) as a function of time (HJD – 2452600), and the temporal deviation spectrum  $\text{TVS}^{-1/2}$  (top) in units of 1/100 of the continuum flux ( $\%F_c$ ) are shown. The dashed line in the top plot indicates the statistical significance for 1 per cent level. In the bottom plots, the positions of the subpeak in the red absorption troughs are indicated with arrows, and they seem to be moving from night to night (see Section 3.2).

The positions of the subpeak were estimated for each spectrum, by applying a quadratic fit to the data points around the subpeak. The results are shown in Fig. 4 as a function of time. The amplitude of the change in the subpeak position is relatively large on the second night compared to those of the first and the third nights. To demonstrate the motion of the subpeak occurred during the second night, we plot the time-averaged ( $\Delta t = 70$  min) spectra in Fig. 5. The figure shows a weak subpeak moving from  $V \sim 170 \text{ km s}^{-1}$  to  $\sim 220 \text{ km s}^{-1}$  during the course of the night.

The subpeak positions were fitted with a function ( $f$ ) in the form of the Fourier series,

$$f(t) = \frac{a_0}{2} + \sum_{n=1}^{n_{\max}} \left\{ a_n \cos\left(\frac{2\pi n}{P}t\right) + b_n \sin\left(\frac{2\pi n}{P}t\right) \right\} \quad (4)$$

where  $t$  and  $P$  are the time of observation and the rotational period of SU Aur respectively, and  $n_{\max} = 3$ . The reasons for choosing the form of the fitting function above are as follows: 1. a simplest possible form is desirable, and 2. the first harmonic terms in the Fourier series might be present if the variation is related with the stellar rotation, 3. the second harmonic terms in the Fourier series might be present if the variation is caused by the tilted-axis magnetospheric accretion model (e.g. see Shu et al. 1994; Johns & Basri 1995), and 4. the third harmonic terms in the Fourier series might be present because the surface Doppler images of SU Aur by Petrov et al. (1996), Mennessier (1997) and Unruh et al. (2004) weakly suggest the presence of cool spots on the surface at three different longitudes which are approximately equally spaced.

The fit with  $n_{\max} = 3$  is shown in Fig. 4 along with the fits with  $n_{\max} = 1$  and  $n_{\max} = 2$  for comparison. In all cases, the fixed period of 2.7 d (Unruh et al. 2004) was adopted. See Table 1 for the summary of the fitting parameters. The figure clearly shows that the fit with  $n_{\max} = 1$  fails to represent the data. On the other hand, the fits with  $n_{\max} = 2$  and  $n_{\max} = 3$  are significantly better.

The two lines ( $n_{\max} = 2$  and  $n_{\max} = 3$ ) are very similar to each other as we can see from the figure and the values of the Fourier coefficients. The contributions of the third harmonic terms ( $a_3$  and  $b_3$ ) are very small compared to the first and the second harmonic terms. To test whether the third harmonic terms should be included in the fitting functions, we have performed an F-test (c.f. Bevington 1969). From the table, the numbers of degree of freedom are  $\nu_2 = 497$  and  $\nu_3 = 495$  for  $n_{\max} = 2$  and  $n_{\max} = 3$  respectively. Using the reduced chi-square values in the table, we find  $F_\chi = \{\chi^2(n_{\max} = 2) - \chi^2(n_{\max} = 3)\} / \chi^2_{\nu_2} = 2$  and  $F = \chi^2_{\nu_2} / \chi^2_{\nu_3} = 1$ . Since  $F_\chi > F$ , the third harmonic terms should be included in the fitting although their contribution is relatively small.

From this analysis we found that the motion of the subpeak in the red absorption trough is possibly associated not only with  $P$ , but also with  $P/2$ . This is consistent with the tilted-axis magnetospheric accretion model mentioned earlier.

In spite of the excellent fits of the data with Fourier series, we should not ignore a possibility that the rather large amplitude of the change in the subpeak position seen on the second night was caused by a single episodic event (e.g. by a temporal and local enhancement of the accretion flow). Assuming conservation of energy, the free-fall time ( $t_{\text{ff}}$ ) of an object from the co-rotation radius ( $r = R_c$ ) of the star to the stellar surface ( $r = R_*$ ) can be written as

$$t_{\text{ff}} = -\frac{1}{V_{\text{esc}}(R_c)} \int_{R_c}^{R_*} \left(\frac{R_c}{r} - 1\right)^{-1/2} dr \quad (5)$$

where  $V_{\text{esc}}(R_c) = (2GM_*/R_c)^{1/2}$ , and  $R_*$  and  $M_*$  are the stellar radius and mass respectively. By evaluating the integral, one obtains

$$t_{\text{ff}} = \frac{R_c}{V_{\text{esc}}(R_c)} \left\{ \frac{\pi}{2} + q^{1/2} (1 - q)^{1/2} - \arcsin(q^{1/2}) \right\} \quad (6)$$



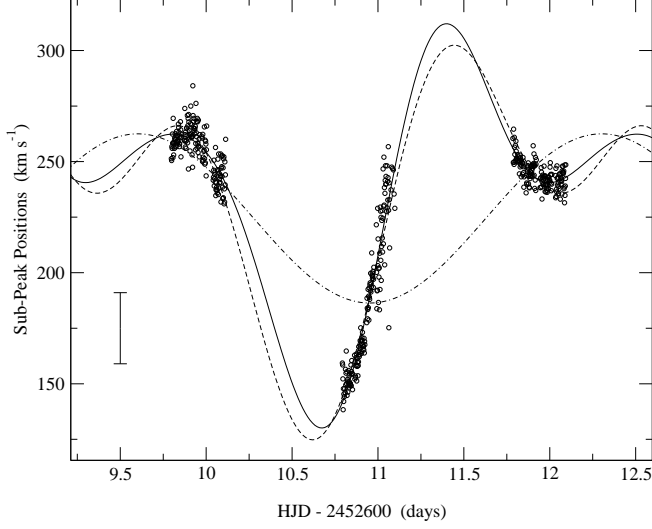


**Figure 4.** The positions of the subpeak (circles) in the red wing of the Pa $\beta$  profile from the three nights are plotted as a function of time. The data were fitted with the Fourier series (equation 4) with the terms up to  $n_{\max} = 1$  (dash-dot line),  $n_{\max} = 2$  (dashed line) and  $n_{\max} = 3$  (solid line). The corresponding fitting coefficients are summarised in Table 1. It is clearly shown that the line with  $n_{\max} = 1$  does not fit the data very well, but the lines with  $n_{\max} = 2$  and  $n_{\max} = 3$  fit the data equally well. The contribution from the third harmonic terms in the Fourier series is very small. The motion of the subpeak in the red absorption trough is associated not only with the rotational period of SU Aur ( $P$ ), but also with half of the period ( $P/2$ ). A typical size of the uncertainty in the peak positions is indicated on the lower-left corner.

where  $q = R_*/R_c$ . Using the mass ( $M_* = 2.25 M_\odot$ ) and the radius ( $R_* = 3.6 R_\odot$ ) of SU Aur from Cohen & Kuhl (1979) along with the co-rotation radius ( $R_c = 3 R_*$ ) in equation 6, we find  $t_{\text{ff}} = 10.5$  h. This time-scale is comparable to the observing time span of a given night, so the association of the subpeak motion on the second night with a single episodic event cannot be ruled out by timescale arguments alone. However, the systematic trends in the acceleration of the feature on the first and third nights strongly suggests that the feature is produced by rotational modulation. To exclude the possibility, the object must be observed for a few rotational periods.

### 3.3 Auto-correlation map

The auto-correlation map for the Pa $\beta$  spectra (with all 503 spectra) was calculated to examine if variability at a given velocity bin is correlated with those at a different part of spectra. The result was placed in Fig. 6 as a greyscale image. The correlation coefficient value ( $C_{ij}$ ) of the  $i$ -th row and the  $j$ -th column in the map was computed by using:

$$C_{ij} = \frac{\sum_{m=1}^N (S_{mi} - \bar{S}_i) (S_{mj} - \bar{S}_j)}{\sum_{m=1}^N (S_{mi} - \bar{S}_i)^2} \quad (7)$$

where  $S_{mn}$  is the signal of the  $n$ -th velocity bin in the  $m$ -th spectrum of the time-series, and  $N$  is the total number of spectra.  $\bar{S}_n$  is the mean signal of the  $n$ -th velocity bin in the time-series. The map is symmetric about the diagonal ( $i = j$  pixels). The range of the correlation values varies from  $-1$  to  $1$  which correspond to a strong anti-correlation and a strong correlation respectively.

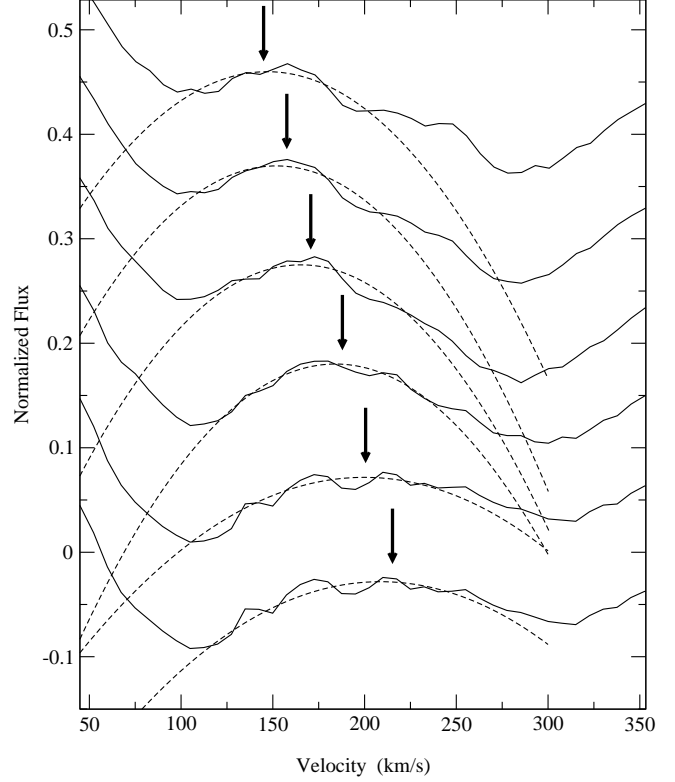


**Figure 5.** The time-series spectra of the Pa $\beta$  from the second night (solid) and the quadratic fits for the subpeak positions (dashed). Each spectrum is the average of 27 consecutive spectra ( $\Delta t = 70$  min) in chronological order from the top to bottom. Each spectrum is vertically displaced by  $-0.1$  from the previous spectrum for clarity. The position of a weak subpeak in the red-wing appears to be moving from  $V \sim 170 \text{ km s}^{-1}$  to  $\sim 220 \text{ km s}^{-1}$  during the course of the second night. The positions of the subpeak were estimated using the original spectra (before being averaged over 27 spectra), by applying a quadratic fit to the data points around the subpeak (Fig. 4). The arrows indicate the measured positions of the subpeak.

The map is useful to visually identify velocity bin regions that correlate or anti-correlate with each other (e.g. Johns & Basri 1995; Oliveira et al. 2000). The figure shows the profile variability in the velocity range ( $-200 \text{ km s}^{-1}, 0 \text{ km s}^{-1}$ ) weakly correlates with that for ( $200 \text{ km s}^{-1}, 400 \text{ km s}^{-1}$ ). On the other hand, they seem to weakly anti-correlate with the variability in ( $0 \text{ km s}^{-1}, 100 \text{ km s}^{-1}$ ). The pattern seen in the map is very similar to that seen in the H $\beta$  auto-correlation function of Oliveira et al. (2000). They also found three similar wavelength ranges in which the flux levels correlate and anti-correlate with one another.

The auto-correlation maps with time lags of  $P/2$ ,  $P/3$  and  $P/4$  where  $P$  is the rotational period were also computed (with  $P = 2.7$  d from Unruh et al. 2004). Because of the poor time coverages (3 nights at a single location) of the data, we were unable to draw any significant conclusion from those maps, and they are not shown here.

### 3.4 Line equivalent width

The line equivalent widths (EWs) of Pa $\beta$  profiles (shown in Fig. 1) are computed by averaging/rebinning over 10 profiles obtained consecutively (approximately over 30 minutes), in order to decrease the size of variance due to the relatively low average S/N

**Table 1.** The summary of the fitting parameters in equation 4 for the positions of the subpeak shown in Fig. 4.  $N$  and  $\chi^2_\nu$  are the number of data points and the reduced chi-square respectively.

$n_{\max}$	$N$	$\chi^2_\nu$	$a_0$	$a_1$	$b_1$	$a_2$	$b_2$	$a_3$	$b_3$
1	503	3.5	224.	-35.7	-13.2	...	...	...	...
2	503	2.8	288.	-46.2	36.6	-36.7	29.9	...	...
3	503	2.8	234.	-42.3	33.9	-39.4	28.2	-9.14	-1.06

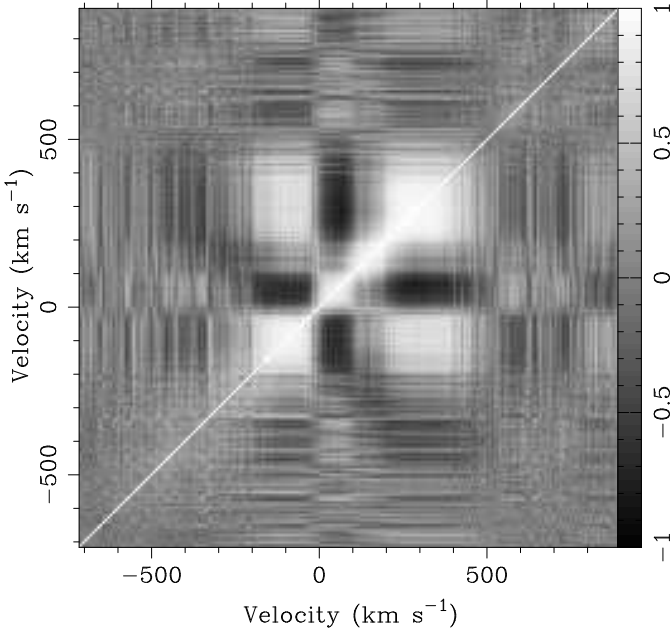


**Figure 6.** Auto-correlation map of the Pa $\beta$  spectra (3 nights) with no time delay. The stronger the correlation, the brighter the pixels in the map. Similarly, the the stronger the anti-correlation, the darker the pixels are. The flux changes seen between  $(-200 \text{ km s}^{-1}, 0 \text{ km s}^{-1})$  and  $(200 \text{ km s}^{-1}, 400 \text{ km s}^{-1})$  are correlated with each other. On the other hand, the flux changes seen between those wavelength ranges weakly anti-correlate with the flux changes seen in  $(0 \text{ km s}^{-1}, 100 \text{ km s}^{-1})$ .

( $\sim 90$ ) in the original profiles. Three different ranges of velocity bins were used for computing the EWs. The total EWs were computed using the velocity range  $-500 \text{ km s}^{-1} < V < 500 \text{ km s}^{-1}$ . The EWs of the red wing (the red EWs) were computed using  $0 \text{ km s}^{-1} < V < 500 \text{ km s}^{-1}$ , and those of the blue wing (the blue EWs) with  $-500 \text{ km s}^{-1} < V < 0 \text{ km s}^{-1}$ . The results are shown in Fig. 7. During the first night, the total EW changes between  $-0.1$  and  $-0.8 \text{ \AA}$ . It changes between  $+0.1$  and  $-0.4 \text{ \AA}$  on the second night, and during the third night it changes between  $-0.7$  and  $-1.9 \text{ \AA}$ . The negative sign in the EW values indicates that the line is in emission. From night to night, the average EW changes from  $-0.4$  to  $-0.2 \text{ \AA}$ , and then to  $-1.5 \text{ \AA}$ .

As we can see from this figure and also from the temporal variance spectra in Fig. 1, the amplitude of the variability for the red wing (or the red EW) is much larger than that for the blue wing; hence, the basic behaviour of the total EW variability follows that of the red wing (the red EW).

According to the figure, the variability of the total EW and that of the red EW appear to be correlated with each other. On other hand, the variability of the total EW and that of the blue wing appear to be anti-correlated for the first and the second night,

but not on the third night. With much larger time steps ( $\sim 1\text{d}$ ), Johns & Basri (1995) found a similar anti-correlation behaviour of the H $\alpha$  EWs measured using the velocity bins  $V \sim -150 \text{ km s}^{-1}$  and those measured using  $V \sim 100 \text{ km s}^{-1}$ . This is consistent with the auto-correlation map (Fig. 6) shown earlier.

The data points were fitted with the Fourier series (equation 4) for  $n_{\max} = 2$  and  $n_{\max} = 3$  cases separately. As done for the fitting of the the subpeak positions in Section 3.2, the period was constrained to be 2.7 d (Unruh et al. 2004) in the fitting procedure. The results are also shown in Fig. 7, and the corresponding Fourier coefficients are summarised in Table 2 along with the reduced chi-square ( $\chi^2_\nu$ ) values.

For all cases (total, red and blue EWs), the lines with  $n_{\max} = 3$  are better representations of the data points, as we can see from the figure and the  $\chi^2_\nu$  values in the table. To test the validity of the statement above, we performed an F-test. For the total EWs fits, the numbers of degrees of freedom are  $\nu_2 = 42$  and  $\nu_3 = 40$  for  $n_{\max} = 2$  and  $n_{\max} = 3$  (Table 2) respectively. Using the values of the reduced chi-square values in the table, we find  $F_\chi = \{\chi^2(n_{\max} = 2) - \chi^2(n_{\max} = 3)\} / \chi^2_{\nu_2} = 37$  and  $F = \chi^2_{\nu_2} / \chi^2_{\nu_3} = 8.1$ ; hence,  $F_\chi > F$ . From this test, we found that the inclusion of the third harmonic terms are a real improvement in the fitting and they should be included. Similar conclusions were found for the blue and the red EW variability curves.

Interestingly, the contribution of the third harmonic terms are as important as the first and the second harmonic terms as one can see from the values of the Fourier coefficients in Table 2. This is consistent with the idea that variation is caused by the combination of the tilted-axis magnetospheric accretion model (for the second harmonic terms) and the presence of the cool spots of the surface at three different longitudes which are approximately equally spaced from the surface Doppler images (for the third harmonic terms), as briefly mentioned in Section 3.2.

Since the data sampling span of one night is very similar to  $P/3$ , it is very difficult to distinguish the  $P/3$  component found in the Fourier analysis from a spurious detection. To overcome this shortcoming, a similar observation must be performed at multiple sites (for continuous phase coverage) for at least a few rotational periods. Also, authors would like to remind readers that the surface Doppler images of SU Aur obtained by Petrov et al. (1996) and Mennessier (1997) suffer from the same data sampling problem as ours. The surface Doppler images constructed by Unruh et al. (2004), on the other hand, are based on the multi-site observations which has a fairly continuous phase coverage and for a few periods; however, they has significant problems with non-periodic line variability.

## 4 MODELS

These data, along with other spectroscopic time-series observations, provide some strong constraints on the possible magneto-

**Table 2.** The summary of the fitting parameters in equation 4 for the equivalent width (EW) data shown in Fig. 7.  $N$  and  $\chi^2_\nu$  are the number of data points and the reduced chi-square respectively. The velocity bins used for the total, red, and blue EWs are  $-500 \text{ km s}^{-1} < V < 500 \text{ km s}^{-1}$ ,  $0 \text{ km s}^{-1} < V < 500 \text{ km s}^{-1}$ , and  $-500 \text{ km s}^{-1} < V < 0 \text{ km s}^{-1}$  respectively.

	$n_{\text{max}}$	$N$	$\chi^2_\nu$	$a_0$	$a_1$	$b_1$	$a_2$	$b_2$	$a_3$	$b_3$
Total	2	48	3.1	-1.20	0.39	-0.06	-0.24	0.41	...	...
Total	3	48	0.4	-0.36	0.59	0.43	-0.52	0.20	0.18	-0.72
Red	2	48	7.2	-1.21	-0.21	0.06	0.29	-0.25	...	...
Red	3	48	0.8	-1.17	-0.22	-0.09	0.26	-0.11	-0.39	0.31
Blue	2	48	0.7	2.38	-0.17	-0.20	0.01	-0.23	...	...
Blue	3	48	0.2	1.55	-0.37	-0.34	0.25	-0.09	0.21	0.39

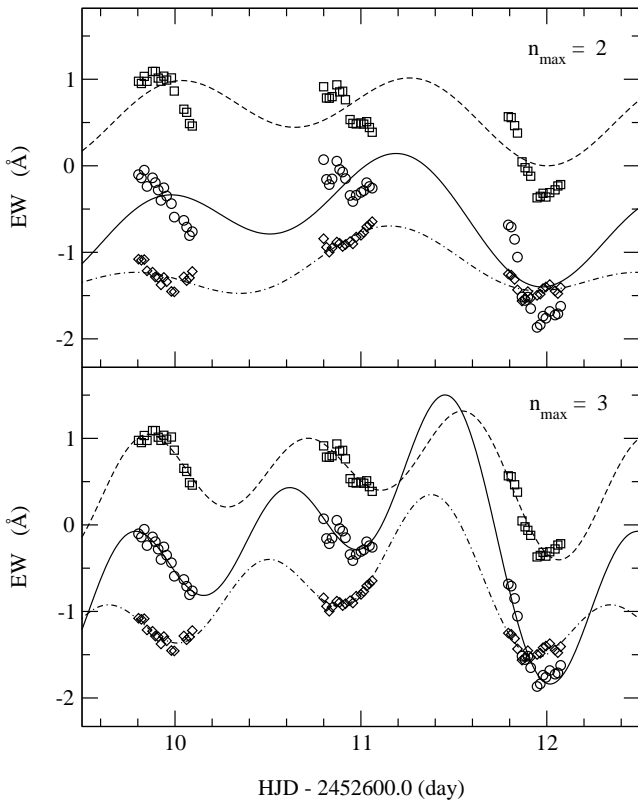


**Figure 7.** The equivalent widths (EW) of Pa $\beta$  using the velocity bins  $-500 \text{ km s}^{-1} < V < 500 \text{ km s}^{-1}$  (circles),  $-500 \text{ km s}^{-1} < V < 0 \text{ km s}^{-1}$  (diamonds) and  $0 \text{ km s}^{-1} < V < 500 \text{ km s}^{-1}$  (squares) are plotted as a function of time. The top panel shows the data fits using equation 4 with  $n_{\text{max}} = 2$ , and the bottom panel shows those with  $n_{\text{max}} = 3$ . The fits for the total EW ( $-500 \text{ km s}^{-1} < V < 500 \text{ km s}^{-1}$ ), the blue EW ( $-500 \text{ km s}^{-1} < V < 0 \text{ km s}^{-1}$ ) and the red EW ( $0 \text{ km s}^{-1} < V < 500 \text{ km s}^{-1}$ ) are shown in solid, dashed and dash-dot lines respectively. The rotational period, 2.7 d (Unruh et al. 2004), was kept constant in the fitting procedure. Table 2 summarises the fitting parameters.

spheric geometry of SU Aur. Specifically, in Section 3.2, we have shown that the motion of the subpeak in the red absorption trough is related not only to the rotational period of the star, but also to half of the rotational period. This phenomenon is consistent with the tilted-magnetic axis models (e.g. see Shu et al. 1994a; Johns & Basri 1995) as mentioned earlier. Furthermore, the analysis in Section 3.4 suggests that the variability of the Pa $\beta$  equivalent width is associated with a half and a third of the rotational period of the

star. This characteristic is also recovered in surface Doppler images by Petrov et al. (1996), Mennessier (1997) and Unruh et al. (2004), and is indicative of the presence of cool spots on the surface at three different longitudes which are approximately equally separated.

To date the observational phenomena associated with SU Aur have been interpreted using cartoon-like models of the circumstellar geometry and dynamics. Although useful, it is not clear that these necessarily simplistic descriptions provide a reasonable explanation of the changes in line-profile shape that are observed. However, it is also true that the near-star geometry is sufficiently complicated that a detailed fit to the observations is not currently tractable, and will probably require a combination of simultaneous time-series observations (spectroscopy, circular polarimetry and photometry) spanning a wide range of wavelength. In this section we adopt a modelling approach that, while falling short of a formal fit, provides a greater quantitative insight into the line profile variability than a cartoon description. Our intention is to develop radiative-transfer models based on the simple magnetospheric geometries that have been proposed in previous studies (Johns & Basri 1995; Petrov et al. 1996). We will be able to determine whether or not these geometries are capable of reproducing the gross characteristics of the line profile variability, and therefore make a better assessment of the applicability of the models.

#### 4.1 The modelling code

The three-dimensional Monte Carlo radiative transfer code TORUS (Harries 2000; Kurosawa et al. 2004; Symington, Harries, & Kurosawa 2004a) is used to compute the Pa $\beta$  line profiles as a function of time (rotational phase). First, the model computes the non-LTE populations of 14-level Hydrogen atoms in the magnetosphere which is funnelling the gas through the magnetic field lines from the inner edge of the accretion disc. Second, the model computes the observed profile of Pa $\beta$  as a function of rotational phase. In our models, the Sobolev approximation (c.f. Mihalas 1978) is used in the framework of core-plus-halo Monte Carlo radiative transfer method, in which the photosphere is treated separately from the outer atmosphere (e.g. accretion streams) of a star. Readers are referred to Symington et al. (2004a) for a detailed description of the spectroscopic model of hydrogen lines arising from the accretion streams in the magnetosphere. All of the accretion flow is assumed to be constant in our models i.e. there is no periodic pulsation of density enhancement etc.

No rotational velocity component is included in our models as it was neglected by Hartmann et al. (1994) and Symington et al. (2004a). The effect of the rotation on Pa $\beta$  is expected to be small according to the calculations of Muzerolle et al. (2001, see

their fig. 8). A slightly larger amount of rotational broadening than that of Muzerolle et al. (2001) is expected for SU Aur since  $v \sin i \sim 60 \text{ km s}^{-1}$  (Johns-Krull 1996; Unruh et al. 2004) while Muzerolle et al. (2001) used  $v \sin i \approx 10 \text{ km s}^{-1}$  in their calculation. Interestingly, Oliveira et al. (2000) found the time-lagged behaviour in the variability of some optical lines, and proposed that this can be caused by the presence of the azimuthal component in the magnetosphere which might be caused by the interaction of the rotating magnetosphere with the circumstellar disc. Although the effect of the rotation on the Pa $\beta$  line may be important for a quantitative measurement, it should not affect the conclusion drawn from the qualitative analysis presented in this section. The exact effect of the rotation on the line formation and variability will be investigated more carefully in a future paper.

#### 4.2 Model configurations

A star with radius  $R_*$  and mass  $M_*$  is placed at the origin ( $O$ ) of a Cartesian coordinate system ( $x, y, z$ ) as shown in Fig. 8. The rotational axis of the star is set to be identical to the  $z$ -axis, and the sense of rotation is counter-clockwise when the star is viewed pole-on. The  $y$ -axis is perpendicular and into the page. An observer is placed on the  $z$ - $x$  plane with an inclination angle  $i$  measured from the  $z$ -axis. The structure of the magnetosphere is the same as that of Hartmann et al. (1994) i.e. the shape of the dipole (poloidal) magnetic field lines is described by

$$r = R_m \sin^2 \theta \quad (8)$$

where  $r$ ,  $R_m$  and  $\theta$  are the radial distance from the centre of the star to a point ( $p$ ) along a field line, the distance to the point where the field line intersects with the equatorial plane, and the polar angle measured from the magnetic axis (normally  $z$ -axis) respectively. The magnetic axis can be inclined by a small angle  $\theta_m$  with respect to the rotational axis. We consider the following three models:

- Model A** A star is surrounded by the axi-symmetric magnetic field (described by equation 8) with constant accretion flow along the magnetic field lines, but the magnetic axis tilted by  $10^\circ$  with respect to the rotational axis.
- Model B** A star is surrounded by the axi-symmetric magnetic field (described by equation 8) except three thin ( $10^\circ$ ) gaps, where there is no magnetic field and gas, are longitudinally placed with equal separations (i.e.  $120^\circ$ ). The magnetic axis is aligned with the rotational axis.
- Model C** A combination of Model A and Model B. The magnetosphere has three  $10^\circ$  gaps, and the magnetic axis is tilted by  $10^\circ$  with respect to the rotational axis.

In all three models, we have adopted the following stellar parameters: the mass  $M_* = 2.25 M_\odot$  and the radius  $R_* = 3.6 R_\odot$  (Cohen & Kuhl 1979). The magnetospheric radius ( $R_m$ ) is assumed to be comparable to the size of the co-rotation radius ( $R_c$ ) of the star (e.g. Pringle & Rees 1972; Ghosh & Lamb 1979; Shu et al. 1994b; Romanova et al. 2002).  $R_c \approx 3.0 R_*$  for  $R_*$  and  $M_*$  values given above. The range of the magnetospheric radius is chosen to be  $R_m = 2.5 - 3.5 R_*$ , which is in proportion to the small/narrow model of Muzerolle et al. (2001). The temperature structure along the magnetic field was adopted from Muzerolle et al. (2001) with the maximum temperature ( $T_{\text{max}}$ ) of 8000 K (see their fig. 2). The stellar continuum of the core star is described by a model atmosphere of Kurucz (1979) with  $T_{\text{eff}} = 5750 \text{ K}$  and  $\log g = 4$  (cgs).

A simple geometrically thin and optically thick accretion disc is placed just outside of the outer edge of the magnetosphere. All

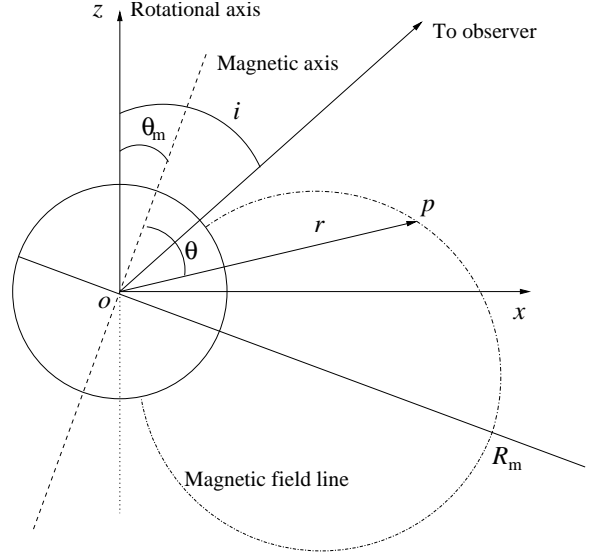


**Figure 8.** Basic model configuration. A star radius  $R_*$  and mass  $M_*$  is placed at the origin ( $O$ ) of a Cartesian coordinate system ( $x, y, z$ ). The rotational axis of the star is identical to the  $z$ -axis, and the sense of rotation is counter-clockwise when the star is viewed pole-on (viewed from  $+z$  direction). The  $y$ -axis is perpendicular and into the page. An observer is placed on the  $z$ - $x$  plane with an inclination angle  $i$  measured from  $z$ -axis. The magnetic axis is tilted by a small angle  $\theta_m$  with respect to the rotational axis. The shape of the dipole (poloidal) magnetic field lines is described by  $r = R_m \sin^2 \theta$  as in e.g. Hartmann et al. (1994).

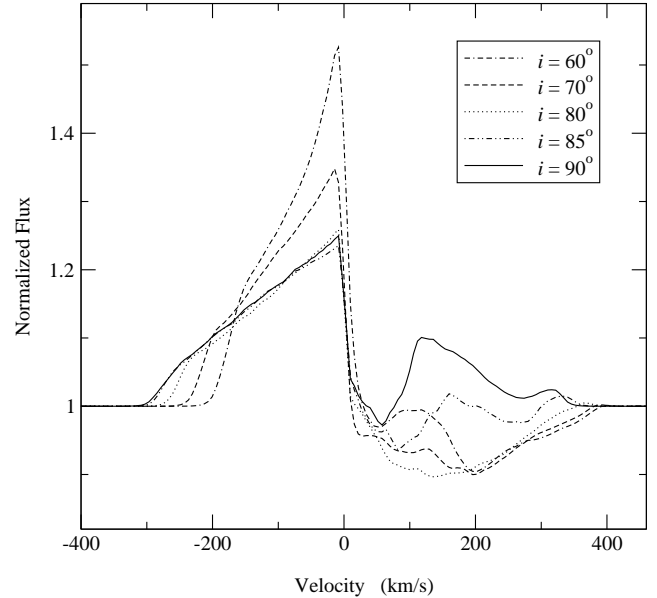


**Figure 9.** The Pa $\beta$  line profiles computed at five different inclinations ( $i = 90^\circ, 85^\circ, 70^\circ, 60^\circ$ ) using the same magnetosphere as in Model A, but without tilting the magnetic axis i.e.  $\theta_m = 0$ . The subpeak in the red wing appears in emission only at the high inclination ( $i > \sim 85^\circ$ ). At lower inclinations ( $i < \sim 70^\circ$ ), the flux level of the blue side of the profile is very sensitive to change in inclination. On the other hand, at higher inclination angles ( $i > \sim 70^\circ$ ), they are insensitive to the change in the inclination angle.



**Table 3.** Model parameters

Model	$\theta_m$ ( $^\circ$ )	# of gaps	$\dot{M}$ ( $10^{-7} M_\odot \text{ yr}^{-1}$ )
A	10	0	1.15
B	0	3	1.25
C	10	3	1.15

the photons which encounter the disc are absorbed. With this assumption of the disc, a photon emitted from the bottom half of the magnetosphere can be occulted by the disc, but a photon emitted from the top half can not be occulted by the disc. This is reasonable for computing Pa $\beta$  profiles except for cases with very high inclination angles. If a more realistic disc (e.g. a flared disc) was used in the model, we would expect the reduction of the photospheric continuum (e.g. Chiang & Goldreich 1999) as well as the line emission due to obscuration by the outer part of the disc. Predicting the exact effects on the line profile shapes caused by this type of obscuration requires modelling of a self-consistent accretion disc, which is beyond the scope of this paper.

Since we do not have the estimate of the amount of the veiling around Pa $\beta$  line, the flux contribution from the disc itself is not considered in our calculations. A recent measurement of the veiling at  $2.2\mu\text{m}$  for *SU Aur* is  $0.6 \pm 0.3$  (Muzerolle et al. 2003), but the value should be significantly smaller at  $1.3\mu\text{m}$  (Pa $\beta$ ). If the veiling correction was taken into account, the line strength of the models presented in this paper would be weaker. The mass-accretion rates ( $\dot{M}$ ) for the models were chosen so that the mean observed line strength is approximately reproduced.

The inclination is set to  $i = 80^\circ$  which is higher than the previously assumed values (e.g. Muzerolle et al. 2003; Unruh et al. 2004). Fig. 9 shows the Pa $\beta$  line profiles computed at different inclination angles using the same magnetospheric accretion structure as in Model A, but with no dipole offset i.e.  $\theta_m = 0$ . At lower inclinations ( $i < \sim 70^\circ$ ), the flux level of the blue side of the profile is very sensitive to changes in inclination. This will cause too much variability in the blue wing if  $\theta_m = 10^\circ$  (as in Model A); hence it will be inconsistent with the observation (c.f. Figs. 1 and 3). On the other hand, at higher inclination angles ( $i > \sim 70^\circ$ ), they are insensitive to the change in the inclination angle. Interestingly, we found that the higher inclination angle ( $i > \sim 85^\circ$  in Fig. 9) is needed to have the subpeak in the red absorption trough in emission (above continuum) as seen in the mean spectra of Pa $\beta$  from the third night of the observation (Fig. 3).

In Models B and C, the locations of the gaps are at the azimuth angles  $105^\circ$ ,  $225^\circ$  and  $345^\circ$  (measured from  $+x$ -axis before tilting) at time  $t = 0$  or equivalently phase = 0. For the models with the tilted magnetic axis (Models A and C), the inclination of the magnetic axis with respect to the observer changes from  $90^\circ$  to  $70^\circ$ , then to  $90^\circ$  as the rotational phase changes from 0 to 0.5, then to 1.0. The model parameters are summarised in Table 3.

### 4.3 Model spectra

We have computed the Pa $\beta$  spectra at 50 different rotational phases, and placed the results in Fig. 10. The figure shows the mean spectra of a whole phase, the deviations from the mean spectra (quotient spectra) as a function of phase in the greyscale image, and the temporal deviation spectra (TVS) $^{-1/2}$  from the models.

The mean spectra of the models broadly reproduce the overall

shape and relative intensity of the observations (Fig. 1), although the model line profiles are rather more triangular. Little difference is seen in the shape of the mean spectra from three models. The models overestimate the levels of the blue-wing (between  $\sim -200$  and  $\sim -100 \text{ km s}^{-1}$ ) compared to the observation. The discrepancy could be caused by e.g. the wrong inclination angle, the wrong geometry of the magnetic field line used in the model, and the fact that the model does not include the rotational velocity component in the accretion streams. If a lower (e.g.  $60^\circ$ ) inclination angle is used, the profile will become less triangular. Although a lower inclination model will give us a better fit to the observed mean profile, the variability in the red absorption trough will be much smaller than that of the observation, and the variability in the blue side will be much larger than that of the observation. The mean spectra from Models A and C show the subpeak in the red absorption trough similar to the one in seen in the observation; however the positions of the subpeak in both models are  $\sim 100 \text{ km s}^{-1}$  smaller than that of the observed spectra.

In Model A, the magnetic axis is perpendicular to the observer when phase = 0. Around this phase, the subpeak in the red absorption trough become most prominent (seen as brighter pixels in the greyscale image). The subpeak arises from a simple geometrical effect: at high inclination the observer's line-of-sight (LOS) towards the hotspots passes through both low velocity material near the disc, and high velocity material near the stellar surface, leading to two absorption components on the red side of the line profile. The relative position and strength of these components changes as the magnetosphere becomes more face-on. The level of the subpeak should become lower as the phase changes from 0 to 0.5 because of this geometrical/projected velocity effect. The greyscale image of Model A shows this effect. Overall line variability seen in the red absorption trough is well reproduced by Models A and C. Since this variability is primarily a geometrical effect, it is quite insensitive to the adopted temperature structure, and we find qualitatively similar behaviour for models with  $6000 \text{ K} < T_{\text{max}} < 10000 \text{ K}$  (although naturally the models differ in detail).

The greyscale image of Model B show the periodic variation (with  $1/3$  of a phase) of the flux levels in the red absorption. The flux level in the red absorption increases as a longitudinal gap approaches the line of sight of the observer since line photons suffer less absorption. Finally, the greyscale of Model C shows a complicated variation pattern, but it is easy to see that the pattern is essentially a combination of the variability patterns from Models A and B.

The temporal deviation spectra of Models A and C reproduce approximately the same range of the line variability ( $-400 \text{ km s}^{-1}$ ,  $500 \text{ km s}^{-1}$ ) as seen in the observations (Fig. 1). Model B does not fit the (TVS) $^{-1/2}$  of the absorption at all. In the (TVS) $^{-1/2}$  of Models A and C, rather large discrepancies are seen in the amount of the variability around the line centre (slightly on the blue side). While the peak of the variability in the red absorption occurs at  $\sim 150 \text{ km s}^{-1}$  for Model A and C, it occurs at  $\sim 275 \text{ km s}^{-1}$  in the observation.

A possible way to shift the peak of the (TVS) $^{-1/2}$  in the red wing (equivalently the position of the subpeak in the mean spectra) to a higher velocity bin is to have a larger magnetospheric radius ( $R_m$ ), in which the accretion gas has higher infalling velocity. Although this means the magnetic accretion streams have to extend beyond the co-rotation radius of the star, this would be still consistent with the magneto-hydrodynamic model of Romanova et al. (2002) who found a torque-less accretion is possible when  $R_m \approx 1.5R_c$  where  $R_c$  is the co-rotation radius of a star.

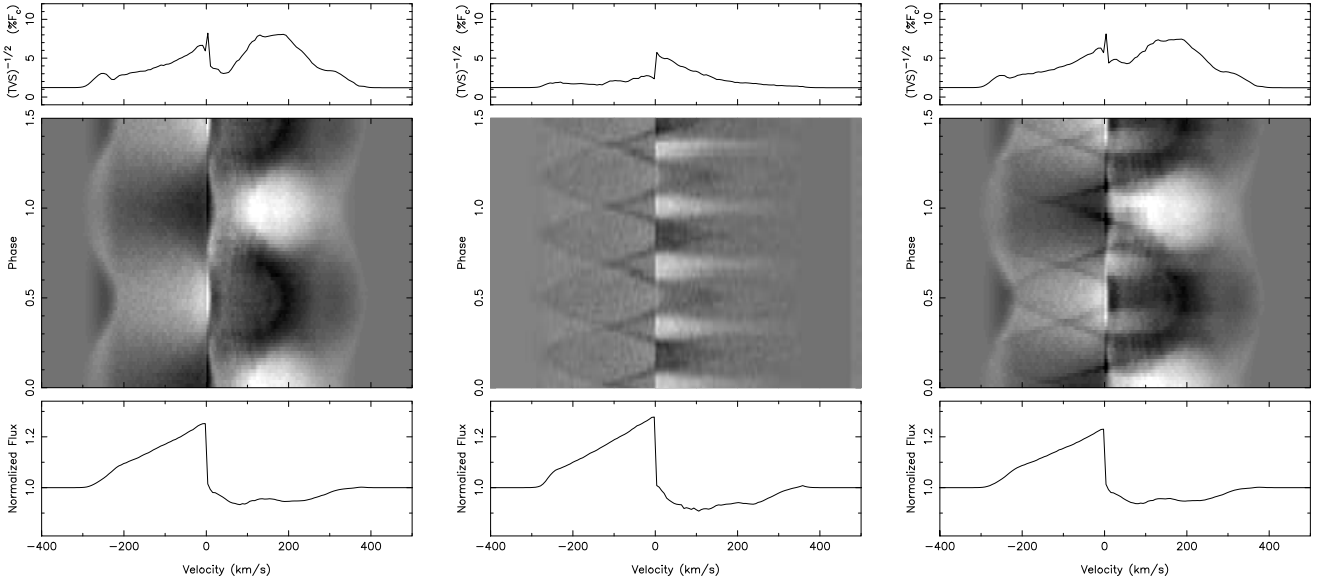


**Figure 10.** The summary of the Pa $\beta$  spectra computed for Model A (left), Model B (centre) and Model C (right). For each model, spectra were computed at 50 different rotational phases. In the bottom panels, the mean spectra of all rotational phases are shown. In the middle panels, the quotient spectra (divided by the mean spectrum) are shown as greyscale images with increasing rotational phases in vertical direction. The greyscale image is scaled from 1.1 (white) to 0.9 (black). The temporal deviation spectra (TVS) $^{-1/2}$  are shown in the top panels. When computing the temporal deviation spectra, the signal-to-noise ratio of 90 (in continuum) was used to match that of the observation (Section 2). See Table 3 for the model parameters adopted.

#### 4.4 Model auto-correlation maps

The auto-correlation maps of Pa $\beta$  line (with no time lag) were computed using the spectra of Models A, B and C, and the results were placed in Fig. 11 along with the auto-correlation map shown in Fig. 6 for a comparison.

In the map for Model A, the changes in the flux levels in the velocity range ( $-200 \text{ km s}^{-1}$ ,  $0 \text{ km s}^{-1}$ ) and ( $0 \text{ km s}^{-1}$ ,  $400 \text{ km s}^{-1}$ ) are strongly correlated with themselves while they are anti-correlated with each other. In other words, as the flux level in ( $-200 \text{ km s}^{-1}$ ,  $0 \text{ km s}^{-1}$ ) increases the flux level in ( $0 \text{ km s}^{-1}$ ,  $400 \text{ km s}^{-1}$ ) decreases, and vice versa.

The blocks of correlation and anti-correlation (seen as black and white squares in the map of Model A) are less pronounced for Model B. The third quadrant block ( $-300 \text{ km s}^{-1}$ ,  $0 \text{ km s}^{-1}$ )  $\times$  ( $-300 \text{ km s}^{-1}$ ,  $0 \text{ km s}^{-1}$ ) of Model B is more complicated than that of Model A because the accretion streams located on the far (back) side of the star (as seen by the observer) will be seen through the gap as it approaches the near (front) side of the star. The map for Model C is essentially the same as that of Model A since the overall variability caused by the presence of the gaps is relatively small compared to that by the precession of the magnetic axis.

The main differences between the auto-correlation map of the observation and the models are: 1. the absence of the anti-correlation between the velocity ranges ( $0 \text{ km s}^{-1}$ ,  $100 \text{ km s}^{-1}$ ) and ( $200 \text{ km s}^{-1}$ ,  $400 \text{ km s}^{-1}$ ) in the models and 2. For Models A and C, the two dark stripes (anti-correlation bands) crossing perpendicular to each other are about two times wider than that of the observation, and they appear as two large dark blocks and two smaller blocks. The total phase coverage of the observation is approximately 1/3 of the whole phase; therefore, this may also contribute to the difference seen in the maps from the observation and the models.

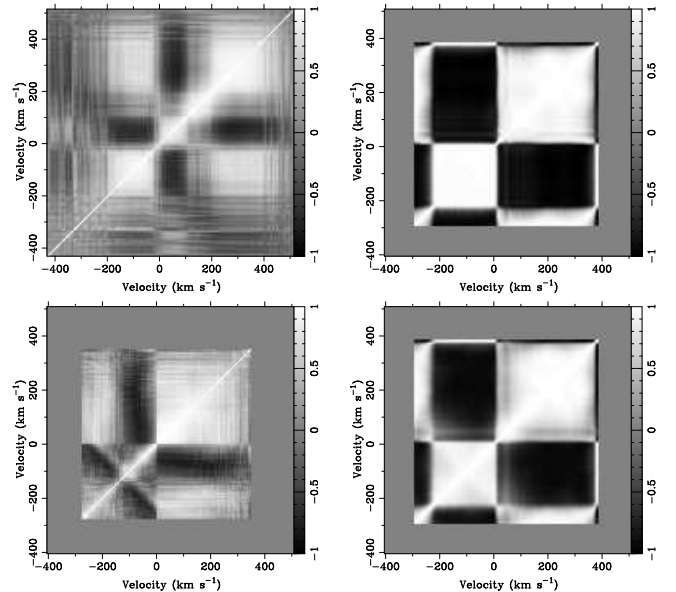


**Figure 11.** Auto-correlation maps of Pa $\beta$  from the observation (upper-left) and from the radiative transfer models: Models A (upper-right), B (lower-left) and C (lower-right). The velocity bins of the continuum are excluded from the model auto-correlation maps, and their values are set to 0 (seen as gray outer frames). No anti-correlation between the velocity ranges ( $0 \text{ km s}^{-1}$ ,  $100 \text{ km s}^{-1}$ ) and ( $200 \text{ km s}^{-1}$ ,  $400 \text{ km s}^{-1}$ ) is seen in the models unlike the observation. The position of the two dark stripes (anti-correlation bands) crossing perpendicular to each other is on the blue side ( $-125 \text{ km s}^{-1}$  and  $-125 \text{ km s}^{-1}$ ) for Models A and C, but it is on the red side ( $100 \text{ km s}^{-1}$  and  $100 \text{ km s}^{-1}$ ), in the observation.

#### 4.5 Motion of the subpeak in the red absorption

In Section 3.2, we found that the motion of the subpeak in the red absorption trough was possibly related with the precession of magnetic axis around the rotational axis. In Fig. 12, a subset (25 out of 50) of Pa $\beta$  line spectra from Model A is shown. Only the red side of the line profiles are shown to emphasise the motion of the subpeak. At phase = 0, the inclination angle of the magnetic axis with respect to an observer is  $90^\circ$ , then it gradually decreases to  $70^\circ$  as the phase reaches to 0.5. The inclination of the magnetic axis increases again to  $90^\circ$  as the phase reaches to 1.

The velocity position of the subpeak moves from  $V \approx 120 \text{ km s}^{-1}$  (at phase = 0) to  $V \approx 200 \text{ km s}^{-1}$  (at phase =  $\sim 0.25$ ), and then to  $V \approx 130 \text{ km s}^{-1}$  (at phase = 0.5). The motion is symmetric about phase = 0.5. As the phase approaches 0.25, the main subpeak feature becomes less pronounced, and it smoothly shifts to a smaller subpeak seen at  $V \approx 130 \text{ km s}^{-1}$  (indicated by an arrow in the figure) as the phase approaches 0.5.

Fig. 13 shows the positions of the subpeak, presented in Fig. 12, as a function of rotational phase. It clearly shows the presence of the second harmonic components as seen in the observation (Fig. 4). At phase around 0.25 and 0.75, the velocity reaches the maximum value ( $V \approx 200 \text{ km s}^{-1}$ ) which is about 1.4 times smaller than the maximum velocity seen in the observation ( $V \approx 280 \text{ km s}^{-1}$ ). At phase = 0 and 1, the velocity reaches the minimum value ( $V \approx 120 \text{ km s}^{-1}$ ) which is comparable to that of the observation ( $V \approx 140 \text{ km s}^{-1}$ ).

In the time-series spectra of Model B, no clear subpeak is seen in the red absorption trough therefore it is not shown here. Model C shows a similar variability pattern of the subpeak as in Model A. The gaps in the magnetosphere in Model B and C, are unlikely the causes of the subpeak motion. From this analysis, we found that the Models A and C reproduce qualitatively similar variability in the red absorption as seen in the observation.

#### 4.6 Line equivalent width variability

Based on the model spectra computed in section 4.3, the EW of Pa $\beta$  were computed using the velocity bins from  $-500 \text{ km s}^{-1}$  to  $500 \text{ km s}^{-1}$ , and plotted as a function of time (Fig. 14). The model phase was multiplied by the period of SU Aur (2.7 d; Unruh et al. 2004), and translated by +9.1 d to match approximately the positions of the peaks in the observed EW variability curve.

According to Fig. 14, the ranges of the EW variation predicted by Models A, B and C are about 0.7, 0.5 and  $0.9 \text{ \AA}$  respectively. On the other hand, the observation (Fig. 7) shows the ranges of 0.7, 0.5 and  $1.2 \text{ \AA}$  for the first, second and third nights. The amplitudes of EW changes predicated by the models are within the range of the observational uncertainty ( $\sim 0.3 \text{ \AA}$ ). A direct comparison between the absolute values of EW would be misleading since our model is not a formal fit to the data. Nonetheless, we note that our model mean EW ( $-1.0 \text{ \AA}$ ) is comparable to the mean EW of the observation ( $-0.7 \text{ \AA}$ ), although of course the observations do not fully sample a complete rotational period.

The overall characteristics of the EW variability seen in the observation is well reproduced by Models A and C, but Model C with three gaps is preferred because it shows both  $P/2$  and  $P/3$  variation found in the observation (section 3.4). Model B is clearly inconsistent with the data. A better match of the observation with Model C can be achieved by carefully choosing the longitudinal position of the gaps with respect to the tilt of the magnetic axis. The amplitude of the EW variability can be increased by using wider

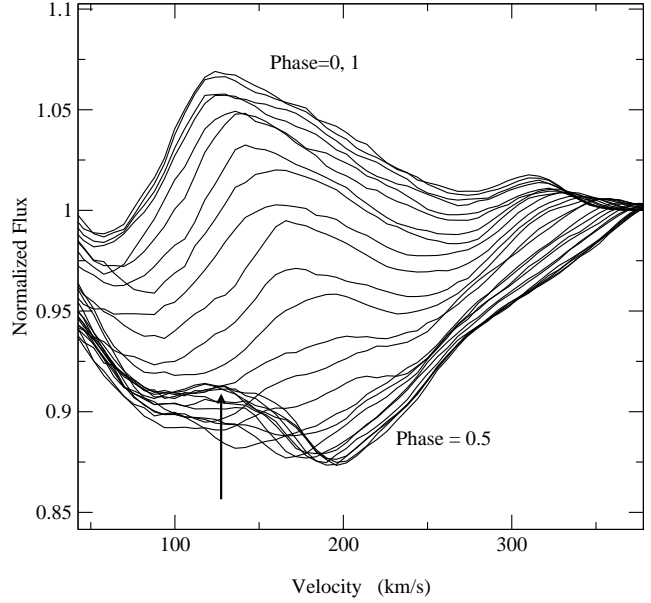


**Figure 12.** The red wings ( $V > 0 \text{ km s}^{-1}$ ) of the Pa $\beta$  spectra from Model A at 25 different rotational phases (0–1). The velocity position of the subpeak moves from  $V \approx 120 \text{ km s}^{-1}$  (at phase = 0) to  $V \approx 200 \text{ km s}^{-1}$  (at phase =  $\sim 0.25$ ), and then to  $V \approx 130 \text{ km s}^{-1}$  (at phase = 0.5). The motion is symmetric about phase = 0.5. As the phase approaches 0.25, the main subpeak feature becomes less pronounced, and it smoothly shifts to a smaller subpeak (indicated by an arrow) seen at  $V \approx 130 \text{ km s}^{-1}$  when the phase is around 0.5. Also see Fig. 13.

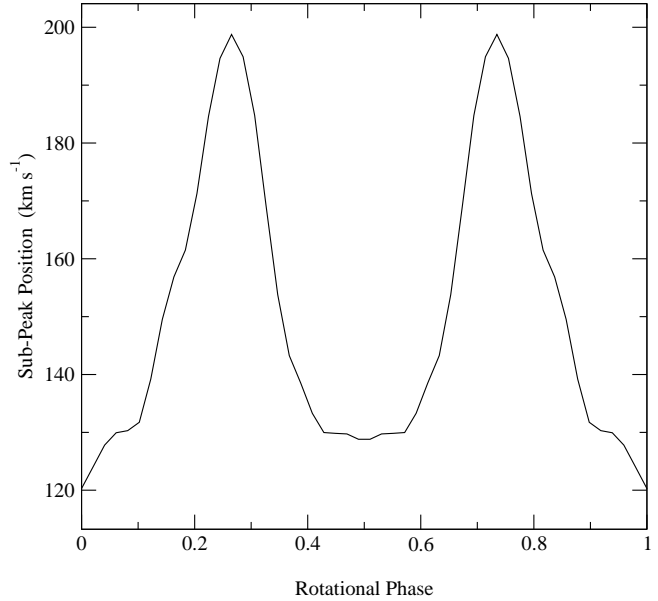


**Figure 13.** The positions of the subpeak in the red wing of the Pa $\beta$  time-series spectra (Model A) shown in Fig. 12 are plotted as a function of rotational phase (0–1). The figure clearly shows the presence of the second harmonic components as seen in the observation (Fig. 4). At phase around 0.25 and 0.75, the velocity reaches the maximum value ( $V \approx 200 \text{ km s}^{-1}$ ) which is about 1.4 times smaller than the maximum velocity seen in the observation ( $V \approx 280 \text{ km s}^{-1}$ ). At phase = 0 and 1, the velocity reaches the minimum value ( $V \approx 120 \text{ km s}^{-1}$ ) which is comparable to that of the observation ( $V \approx 140 \text{ km s}^{-1}$ ).

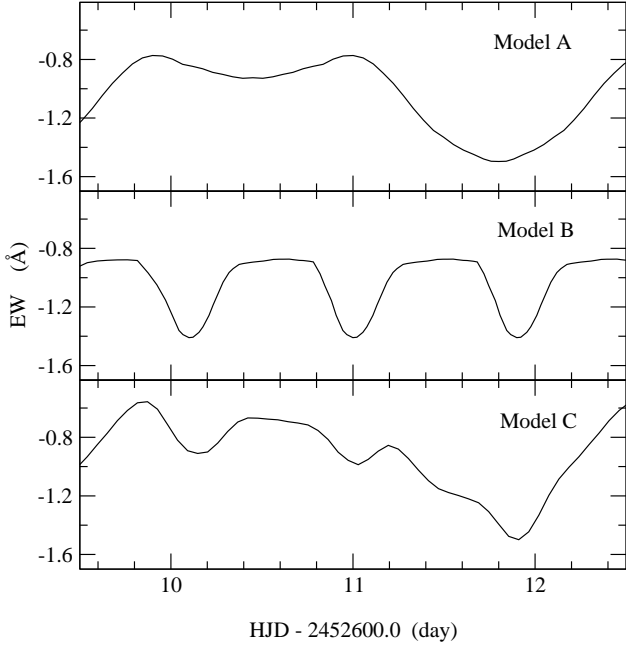


**Figure 14.** The equivalent widths (EWs) of Pa $\beta$  as a function of time from Model A (top), Model B (middle), and Model C (bottom). The model phase was multiplied by the period of SU Aur (2.7 d; Unruh et al. 2004), and then translated by +9.1 d to match the peaks of the observed EW. Models A and C reproduced the overall characteristics of the EW variability seen in the observation (see Fig. 7), but Model B does not.

gaps in the magnetosphere, and by increasing the tilt angle of the magnetic axis.

Interestingly, the recent light curve calculation of Romanova et al. (2004), who considered the flux variation caused by the hot spots on the surface of the rotating stars in their magneto-hydrodynamic simulations, showed the presence of second harmonic (two peaks in one rotational period) when the inclination angle ( $i > 75^\circ$ ). This is consistent with the EW curve of our Model A.

## 5 CONCLUSIONS

We have presented the 503 time-series echelle spectra of Pa $\beta$  line of SU Aur (Fig. 1). From the temporal variance spectra analysis (Section 3.1), we found that the line displayed relatively strong variability within the velocity range ( $100 \text{ km s}^{-1}$ ,  $420 \text{ km s}^{-1}$ ) in the red absorption trough, and weak variability within the velocity range ( $-200 \text{ km s}^{-1}$ ,  $0 \text{ km s}^{-1}$ ) in the blue wing while the flux level at the line centre remained almost constant. A hint of blue-shifted absorption at about  $-150 \text{ km s}^{-1}$  was found on the second night. Interestingly, a similar blue-shifted absorption feature at  $-150 \text{ km s}^{-1}$  are seen in H $\alpha$  and H $\beta$  profiles, which modulates with the rotational period of the star (Giampapa et al. 1993; Johns & Basri 1995).

We found the presence of a subpeak in the red absorption trough in each spectra (Fig. 3), and its position changes in time (Fig. 4). The variability seen in the red-wing seems to be caused mainly by the motion of this subpeak. The position of the peak was fitted well with the Fourier series summed up to the second harmonic term ( $n_{\text{max}} = 2$  in equation 4), indicating that the variability is associated not only with the rotational period but also a half

of the rotational period. This is consistent with the tilted-axis magnetospheric accretion models (e.g. Shu et al. 1994a; Johns & Basri 1995). To exclude the possibility that the large amplitude of the change in the subpeak position seen on the second night was caused by a single episodic event, the object must be observed for a few rotational periods.

The auto-correlation map (Fig. 6) showed the profile variability in the velocity range ( $-200 \text{ km s}^{-1}$ ,  $0 \text{ km s}^{-1}$ ) weakly correlates with that for ( $200 \text{ km s}^{-1}$ ,  $400 \text{ km s}^{-1}$ ). The variability in those two velocity ranges weakly anti-correlates with the variability in ( $0 \text{ km s}^{-1}$ ,  $100 \text{ km s}^{-1}$ ). The map is very similar to that seen in the H $\beta$  auto-correlation function shown by Oliveira et al. (2000).

The modulations of the line equivalent widths (EW) (Fig. 7) are fitted well with the Fourier series (equation 4) summed up to the third harmonic terms ( $n_{\text{max}} = 3$  in equation 4), indicating that the modulations might be associated not only with the rotational period of SU Aur and a half of the period, but also a third of the period. Because our data sampling period and the  $P/3$  component of the Fourier analysis are very similar to each other, it is possible that the detection of the  $P/3$  contribution may be spurious. A definitive observation requires a multi-site campaign to continuously monitor the object for at least two rotational periods.

From the comparison of the observation with the radiative transfer models (Models A, B and C in Section 4), we have learnt the followings:

1. The inclination angle (with respect to the magnetic axis) must be rather high ( $\sim 85^\circ$ ) to have the subpeak (in the red wing) in emission as seen in the mean observed profile from the third night (see Figs. 3 and 9). If a more realistic accretion disc was used in our model, instead of the geometrically thin and opaque disc, this angle would most likely change. At the lower inclination angles ( $i < \sim 70^\circ$ ), the models will overestimate the variability in the blue wing when compared to the observation. Since the profile shape highly depends on the geometry of the magnetosphere, these conclusions would change if the geometry other than the one in Hartmann et al. (1994) is used.

2. The tilted magnetic axis models (Models A and C) reproduce the temporal deviation spectra (TVS) $^{-1/2}$  which have similar ranges and shapes as seen in the observation (Fig. 10). On the other hand, the mean spectra of the models (A, B and C) are more asymmetric and triangular than the observed profile. The discrepancies may arise from several simplifying assumptions in the model, in particular the adoption of Sobolev line transfer (which is a poor approximation at the line centre) and the neglect of turbulent broadening.

3. The motion of the subpeak in the red absorption trough seen in the observation (Figs. 3 and 4) was qualitatively reproduced by the tilted magnetic axis models (Models A and C). See Fig. 12. The models reproduced the motion of the subpeak with the second harmonic components (associated with  $P/2$  where  $P$  is the rotational period), as seen in the observation.

4. The tilted magnetic axis models with the gaps in the magnetosphere (Models C) predicts the line equivalent width (EW) variability patterns very similar to that seen in the observation (Figs. 7 and 14). The model shows the  $P/2$  and  $P/3$  variability of the EWs as seen in the observation.

The models presented here represent the next step in quantifying the magnetospheric geometry of T Tauri stars, moving from purely qualitative descriptions of the circumstellar environment to a more quantitative approach. The complex nature of the problem, with inflowing and outflowing material, non-axisymmetric (and possibly non-stationary) accretion, render a formal fit to the data



extremely difficult. Further progress will only be possible with an extensive, coordinated observational programme, spanning a variety of techniques and wavebands. Zeeman Doppler Imaging (ZDI; Semel et al. 1993) of the surface magnetic field topology would provide strong constraints on the magnetospheric geometry, particularly when combined with photometric time-series. Simultaneous  $H\alpha$  and  $\text{Pa}\beta$  spectroscopy would also be extremely useful, since  $H\alpha$  appears to be a good tracer of outflow emission, while we have shown that  $\text{Pa}\beta$  probes the accretion streams. Time-series  $H\alpha$  linear spectropolarimetry may also provide useful new insights (Vink et al. 2003; Vink et al. 2004).

## ACKNOWLEDGEMENTS

We would like to thank the anonymous referee for constructive comments and suggestions for improving the clarity of the manuscript. We also thank the staff of the JAC, and Paul Hirst in particular, for their help in obtaining the observations. RK thanks Stuart Littlefair for help with data reduction. RK is supported by PPARC standard grand PPA/G/S/2001/00081.

## REFERENCES

- Akeson R. L., Ciardi D. R., van Belle G. T., Creech-Eakman M. J., 2002, *ApJ*, 566, 1124
- Appenzeller I., Mundt R., 1989, *A&AR*, 1, 291
- Basri G., Batalha C., 1990, *ApJ*, 363, 654
- Bertout C., Basri G., Bouvier J., 1988, *ApJ*, 330, 350
- Bevington P. R., 1969, *Data reduction and error analysis for the physical sciences*. McGraw-Hill, New York
- Bouvier J., Cabrit S., Fernandez M., Martin E. L., Matthews J. M., 1993, *A&A*, 272, 176
- Chakraborty A., Ge J., 2004, *AJ*, 127, 2898
- Chiang E. I., Goldreich P., 1999, *ApJ*, 519, 279
- Cohen M., Kuhi L. V., 1979, *ApJS*, 41, 743
- Collier Cameron A., Campbell C. G., 1993, *A&A*, 274, 309
- Edwards S., Cabrit S., Strom S. E., Heyer I., Strom K. M., Anderson E., 1987, *ApJ*, 321, 473
- Edwards S., Hartigan P., Ghandour L., Andrulis C., 1994, *AJ*, 108, 1056
- Folha D. F. M., 1998, PhD thesis, Univ. London
- Folha D. F. M., Emerson J. P., 2001, *A&A*, 365, 90
- Fullerton A. W., Gies D. R., Bolton C. T., 1996, *ApJS*, 103, 475
- Ghosh P., Lamb F. K., 1979, *ApJ*, 232, 259
- Giampapa M. S., Basri G. S., Johns C. M., Imhoff C., 1993, *ApJS*, 89, 321
- Grady C. et al., 2001, *BAAS*, 33, 1396
- Guenther E. W., Emerson J. P., 1996, *A&A*, 309, 777
- Gullbring E., Hartmann L., Briceno C., Calvet N., 1998, *ApJ*, 492, 323
- Harries T. J., 2000, *MNRAS*, 315, 722
- Hartigan P., Edwards S., Ghandour L., 1995, *ApJ*, 452, 736
- Hartmann L., Hewett R., Calvet N., 1994, *ApJ*, 426, 669
- Herbig G. H., 1960, *ApJS*, 4, 337
- , 1962, *Advances in Astronomy and Astrophysics*, 1, 47
- Herbig G. H., Bell K. R., 1988, *Catalog of emission line stars of the orion population*, Vol. 3. Lick Observatory Bulletin, Santa Cruz: Lick Observatory
- Herbst W., Herbst D. K., Grossman E. J., Weinstein D., 1994, *AJ*, 108, 1906
- Horne K., 1986, *PASP*, 98, 609
- Johns C. M., Basri G., 1995, *ApJ*, 449, 341
- Johns-Krull C. M., 1996, *A&A*, 306, 803
- Johns-Krull C. M., Valenti J. A., Hatzes A. P., Kanaan A., 1999, *ApJ*, 510, L41
- Johns-Krull C. M., Gafford, 2002, *ApJ*, 573, 685
- Kenyon S. J., Hartmann L., 1987, *ApJ*, 323, 714
- Kenyon S. J. et al., 1994, *AJ*, 107, 2153
- Koenigl A., 1991, *ApJ*, 370, L39
- Kuhi L. V., 1964, *ApJ*, 140, 1409
- Kurosawa R., Harries T. J., Bate M. R., Symington N. H., 2004, *MNRAS*, 351, 1134
- Kurucz R., 1979, *ApJS*, 40, 1
- Mennessier C., 1997, in *IAU Symp.* Vol. 182, *Herbig-Haro Flows and the Birth of Stars*, Malbet F., Castets A., eds., Kluwer, Dordrecht, p. 300
- Mihalas D., 1978, *Stellar atmospheres*, 2nd edn. W. H. Freeman and Co., San Francisco
- Muzerolle J., Calvet N., Hartmann L., 2001, *ApJ*, 550, 944
- Muzerolle J., Calvet N., Hartmann L., D'Alessio P., 2003, *ApJ*, 597, L149
- Nakajima T., Golimowski D. A., 1995, *AJ*, 109, 1181
- Oliveira J. M., Foing B. H., van Loon J. T., Unruh Y. C., 2000, *A&A*, 362, 615
- Petrov P. P., Gullbring E., Ilyin I., Gahm G. F., Tuominen I., Hackman T., Loden K., 1996, *A&A*, 314, 821
- Pringle J. E., Rees M. J., 1972, *A&A*, 21, 1
- Puxley P. J., Beard S. M., Ramsay S. K., 1992, in *ESO Conf. Proc.*, Vol. 41, 4th ESO/ST-ECF Data Analysis Workshop, Grosbol P. J., de Ruijsseche R. C. E., eds., ESO, Garching, p. 117
- Romanova M. M., Ustyugova G. V., Koldoba A. V., Lovelace R. V. E., 2002, *ApJ*, 578, 420
- , 2004, *ApJ*, 610, 920
- Semel M., Donati J.-F., Rees D. E., 1993, *A&A*, 278, 231
- Shu F. H., Najita J., Ostriker E., Wilkin F., Ruden S., Lizano S., 1994a, *ApJ*, 429, 781
- Shu F. H., Najita J., Ruden S. P., Lizano S., 1994b, *ApJ*, 429, 797
- Symington N. H., Harries T. J., Kurosawa R., 2004a, *MNRAS*, in press
- Symington N. H., Harries T. J., Kurosawa R., Naylor T., 2004b, *MNRAS*, (submitted)
- Uchida Y., Shibata K., 1985, *PASJ*, 37, 515
- Unruh Y. C. et al., 2004, *MNRAS*, 348, 1301
- Valenti J. A., Basri G., Johns C. M., 1993, *AJ*, 106, 2024
- Vink J. S., Drew J. E., Harries T. J., Oudmaijer R. D., Unruh Y. C., 2003, *A&A*, 406, 703
- , 2004, *MNRAS*, in preparation
- Whelan E. T., Ray T. P., Davis C. J., 2004, *A&A*, 417, 247